

Multi-axis inertial sensing with 2D arrays of Bose Einstein Condensates

K. Stolzenberg, C. Struckmann, S. Bode, R. Li, A. Herbst,
V. Vollenkemper, D. Thomas, E. M. Rasel, N. Gaaloul, and D. Schlippert*
*Leibniz Universität Hannover, Institut für Quantenoptik,
Welfengarten 1, 30167 Hannover, Germany*
(Dated: March 14, 2024)

Atom interferometers are an exquisite measurement tool for inertial forces. However, they are commonly limited to one single sensitive axis, allowing high-precision multi-dimensional sensing only through subsequent or postcorrected measurements. Here, we introduce a novel 2D-array-arrangement of Bose-Einstein Condensates (BEC) initialized utilizing time-averaged optical potentials for simultaneous multi-axis inertial sensing. Deploying a 3×3 BEC array covering 1.6 mm^2 , we perform measurements of angular velocity and acceleration of a rotating reference mirror, as well as a linear acceleration, e.g., induced by gravity, gradients, and higher order derivatives. We anticipate increased sensitivity of our method in interferometers with large scale factors in long-baseline or satellite atom interferometry. Our work paves the way for simple high-precision multi-axis inertial sensing and we envision further applications, e.g., for three-dimensional wave front characterization.

Introduction - Atom interferometry allows to determine a wide range of measurable inertial observables, e.g., linear accelerations [1], gravity gradients and curvature [2–4], or rotation rates [5–8]. However, standard atom interferometers are operated with only a single sensitive axis allowing the measurement of only one acceleration or one rotation component. Extending them to multi-dimensional inertial sensors normally requires significant efforts and additional sensitive axes [9–13]. To meet these challenges, 1D-arrays of Bose-Einstein Condensates (BEC) have been introduced in magnetic lattices [14] and optical tweezers [15], to be used as the input of an atom interferometer [16]. These simultaneous atom interferometers allow the reconstruction of the acceleration and rotation components in a single measurement.

In this work, we present a method to create 2D-BEC arrays with scalable dimensionality and spacing of up to 3×3 across 1.6 mm^2 (cf. Figure 1) utilising the exquisite control of time-averaged optical potentials [17–19]. By using the array as a source for 1D-double Bragg diffraction [20] we create up to 9 strongly correlated interferometers benefiting from common-mode rejection and can extract linear accelerations, angular velocities and angular accelerations simultaneously. While similar measurements would theoretically be possible with large atomic clouds and comparisons of different sections (e.g., left and right half of the cloud), reaching baselines on the order of millimeters as demonstrated here would require unfavourably macroscopic clouds. Likewise, our approach allows us to exploit the excellent mode features and low expansion rate of BECs. Beyond the scope of this work, the large number of single, correlated measurements with BEC arrays opens perspective towards high spatial-resolution wave front characterisation and in-situ electromagnetic field measurements.

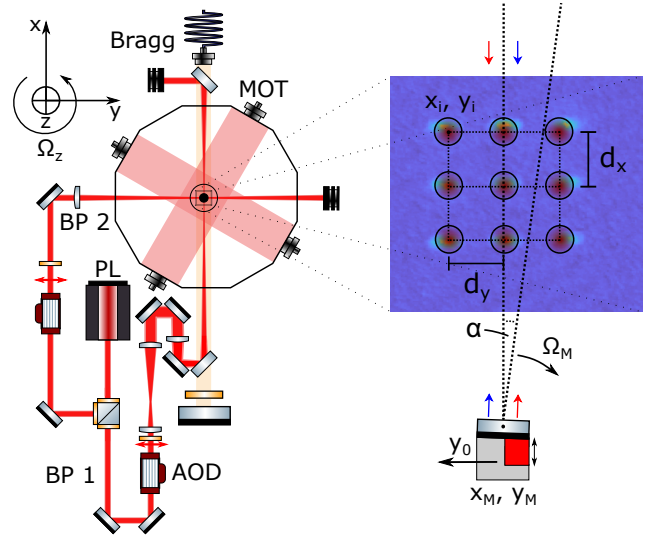


FIG. 1. Experimental setup: Top view of the experimental setup highlighting the ODT setup. g is aligned with z . The two dipole trap beams intersect with an angle of $\sim 90^\circ$ and the two beam paths BP1/2 are depicted. The two AODs in the beam paths allow for dynamically deflecting the laser beams and a 2D-array of potential wells is established. The Bragg beam is aligned with BP1 and split at a dichroic mirror. The retroreflection mirror of the Bragg beam is placed on a translation stage movable in y direction. On the top right an absorption image of a 3×3 array is depicted as well as the piezo, tilting the retroreflection mirror by the angle α . The shift y_0 is only applied in the measurement Fig. 4.

For demonstration and characterization, we imprint angular velocity and acceleration on the atoms by tilting the retroreflection mirror used for Bragg atom optics with a piezo throughout the interferometer sequence. Observables are accessible via phase scans as well as differentially through linear combinations of individual interferometers. The sensitivity to angular velocity and

* schlippert@iqo.uni-hannover.de

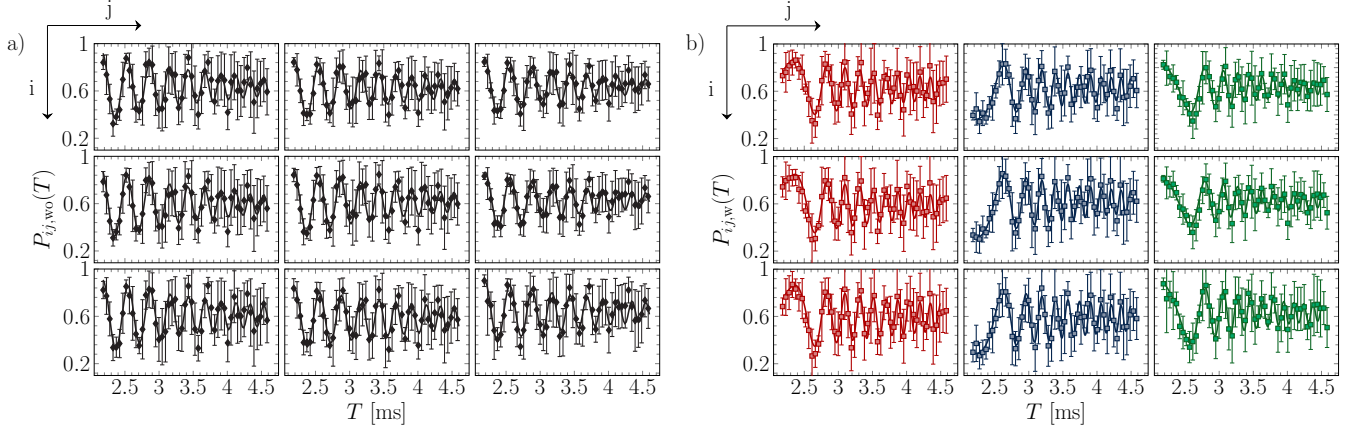


FIG. 2. T scans of a 3×3 -array with and without the induced tilting of the retro reflection mirror: a/b) Fringes obtained for the 9 simultaneous atom interferometers for $T = 2.182 - 4.582$ ms. a/b) correspond to data acquired without/with induced rotation.

acceleration originates from the combination of two or more 1D-measurements separated by a scalable baseline, in analogy with inertial-stabilized platforms [21] or as proposed for the combination of atom interferometers [22]. The baselines utilized in this work are on the order of ~ 1 mm. We envisage applications of our method in very long baseline atom interferometry facilities [23–25] or on satellites [26] with significantly increased scale factors.

Phase sensitivity - A detailed description of the production, state preparation and transport of the BEC-array and the interferometry setup is given in the supplemental material I. The phase response of the atom interferometer is subject to all inertial forces acting on the reference mirror. Rotational effects induce phase shifts scaling with the initial kinematics of the atoms and thus, are of special interest here. The atoms are prepared with initial positions (x_{ij}, y_{ij}) in a 2D-plane with negligible initial velocity. It is sufficient to consider rotations of the mirror as a demonstration of the sensor as they directly correspond to rotations of the lab frame. Here, we consider rotations with constant angular acceleration around the y -axis (see Figure 1), $\alpha_M(t) = \alpha_{M,0} + \Omega_M(t - T) + \frac{1}{2}\dot{\Omega}_M(t - T)^2$, sampled around the temporal center of the atom interferometer sequence corresponding to the interrogation time T . Furthermore, we choose the sensitive axis perpendicular to the gravitational acceleration g up to a slight tilt θ_g . Following the approach demonstrated in Refs. [13, 27], the leading order phase terms are given by

$$\phi_{ij} = 2k_{\text{eff}}T^2[a_{x,ij} + (y_{ij} - y_M)\dot{\Omega}_M + 2(x_{ij} - x_M)(\Omega_M^2 + \frac{7}{2}\dot{\Omega}_M^2T^2)] \quad (1)$$

where $a_{x,ij} = g_{ij} \sin(\theta_{g_{ij}})$ and (x_M, y_M) denotes the reference mirror's center of rotation. We further neglected phase shifts induced by Earth's rotation rate as

we operate in very short times, $T < 5$ ms. By a slightly accelerated tilting of the mirror in 12.5 ms (cf. Fig. 3 d)), we measure rotation rates of $\Omega_M \sim 0.1 \text{ rad s}^{-1}$ and angular accelerations of $\dot{\Omega}_M \sim 10 \text{ rad s}^{-2}$.

Rotation measurement - For measuring the rotations induced by the mirror, we initialize a 3×3 array with spatial separation of $(d_x, d_y) = (1.0, 0.435)$ mm. We subsequently release the BECs from the crossed optical dipole trap (ODT) and start of the interferometer sequence after 1 ms of free fall. We scan the interrogation time T from 2.182 to 4.582 ms in 20 equidistant steps to fit the phase in post processing. To isolate the rotational effects, for each T , we measure the port population with and without the mirror rotation. The resulting fringes are shown in Fig. 2 a) and b), respectively. The signal under consideration is the normalized population $P_{ij} = N_{ij, \pm 2\hbar k_{\text{eff}}} / N_{ij, \text{tot}}$ of the $\pm 2\hbar k_{\text{eff}}$ states which is of the form,

$$P_{ij}(T) = P_{ij,0} + \frac{1}{2}C_{ij} \times \sin(\phi_{ij}(T) + \phi_0) \quad (2)$$

where $P_{ij,0}$ denotes a population offset, C_{ij} the contrast of the interferometer and ϕ_0 a constant phase offset. ϕ_{ij} is the phase given in eq. (1). The objective is to derive the inertial effects, comprising linear acceleration $a_{x,ij}$, rotation rate $\Omega_M(T)$, and angular acceleration $\dot{\Omega}_M(T)$, from the population signal. Both the angular velocity and acceleration are time dependent, and, thus, a function of the interrogation time T . Assuming a non-rotating mirror, the phase shift simplifies to $\phi_{ij}|_{\alpha=0} = 2k_{\text{eff}}T^2a_{x,ij}$. A fit of the associated fringes $P_{ij}|_{\alpha=0}$ has shown $\phi_0 = 0.4\pi$ and $a_{x,ij} = (0.1111(7), 0.1113(6), 0.1109(6), 0.1109(7), 0.1117(6), 0.1111(6), 0.1112(7), 0.1119(6), 0.1107(6)) \text{ m s}^{-2}$ for the 9 interferometers top left to bottom right (see Fig.2 a)). Due to the fact that the Bragg pulses were optimised for a rotating mirror deflecting the beam by ~ 1 mm, the

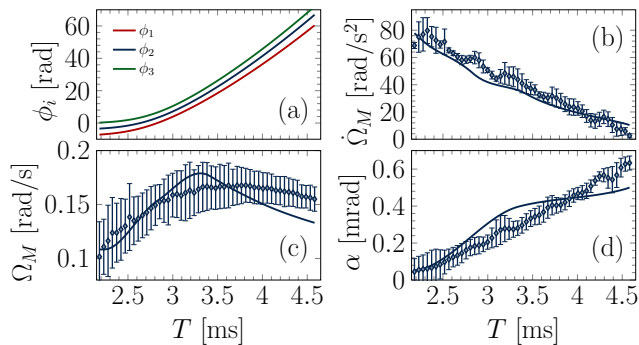
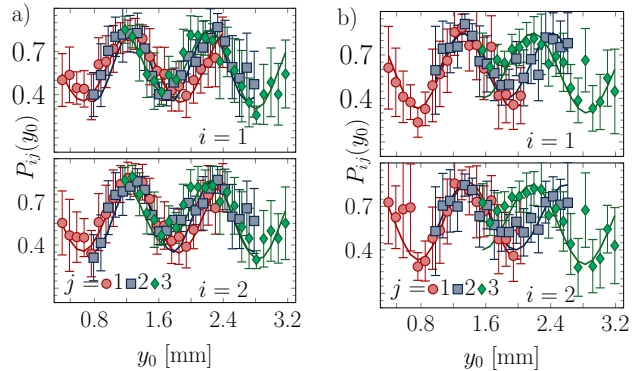


FIG. 3. Result of fitting the relative populations compared to a direct measurement. The measurement data points are received by averaging over five repeated measurements. The fit is given as a solid line. The phase shift extracted from $P_j(T)$ averaged over the rows i is given for every column j in (a). By taking the difference of two phases ϕ_j , the angular acceleration $\dot{\Omega}_M$ is obtained in (b). Further, constraining $\Omega_M = (\alpha(0) + \alpha(2T))/(2T)$ to be consistent with the sampling of its derivative, $\dot{\Omega}_M = (\alpha(0) - 2\alpha(T) + \alpha(2T))/T^2$, allows the extraction of the angular velocity Ω_M in (c). With this the time series of the mirror angle can be reconstructed up to a constant offset in (d). Ω_M and $\dot{\Omega}_M$ were determined using $x_M = 0.25$ m and $y_M = 1.5$ mm.

interferometers with no mirror rotation incorporate an additional frequency leading to alternating visibility with each oscillation. This is owed to unfavorable efficiency of the beam splitting pulse, creating effectively single Bragg interferometers [28]. The interferometers performed with a rotating mirror show signals $P_{ij}(T)$ whose phase is given by eq. (1). To extract the time-dependent phase, we consider small intervals of 500 μs where the phase is assumed to be constant. We then move this interval over the whole dataset, receiving estimations of the acceleration signal at the mean time t of the interval, $a_{ij}(t) = \phi_{ij}(t)/(2k_{\text{eff}}t^2)$. To obtain the correct continuous phase from the set of partially constant accelerations, we integrate over temporal acceleration changes, $\phi_{ij}(t) = \phi_{ij,0} + 2k_{\text{eff}} \int_0^t (2a_{ij}(\tau)\tau + a'_{ij}(\tau)\tau^2) d\tau$. The phase information of every BEC in the grid, ϕ_{ij} , then can be used to directly extract the angular velocity and angular acceleration by taking the row-wise and column-wise differences, respectively. For the measurements performed here, the mirror's rotation is dominated by the angular acceleration, whereas the angular velocity is too small to be visible in the differential signal. This is evident from the fringes depicted in Figure 2 b), where no row-wise phase shift is observable, yet a clear phase shift is evident column-wise. Thus, we are only able to extract the angular acceleration by taking the column-wise difference of the phases $(\phi_{i,j} - \phi_{i,j+1})/(2k_{\text{eff}}T^2d_y) = \dot{\Omega}_M$. The angular velocity needs to be extracted from the nominal signal scaling with x_M , requiring a preceding measurement of the linear acceleration $a_{x,ij}$. Using the measurement of $a_{x,ij}$



(a) $(d_{x,1}, d_{y,1}) = (870, 390)\mu\text{m}$ (b) $(d_{x,2}, d_{y,2}) = (870, 580)\mu\text{m}$

15.8(6)	20.0(6)	17.3(6)	16.3(12)	17.8(11)	24.0(9)
16.0(6)	19.5(6)	17.1(6)	15.8(12)	15.9(11)	12.0(9)

(c) $\dot{\Omega}_M$ from (a) in rad s^{-2} (d) $\dot{\Omega}_M$ from (b) in rad s^{-2}

FIG. 4. Linear phase scans by displacing the retro reflection mirror & differential plots of the data for a 2×3 array: The fringe scans $P_{ij}(y_0)$ for $T = 3.2$ ms obtained by linearly displacing the retro reflection mirror by y_0 are given in (a) for $d_y = 580 \mu\text{m}$ and in (b) for $d_y = 390 \mu\text{m}$. We overlap the signals of each column to showcase the column-wise agreement of the fringe scan's phase and frequency (different colors), $P_{i,j}(y_0 + d_y) = P_{i,j+1}(y_0)$. The resulting angular accelerations from fitting the fringes in (a) and (b) (solid lines) are listed in (c) and (d), respectively. The angular acceleration of the last column in (c) is smaller than the others, caused by clipping of the Bragg-beam at the dichroic mirror. The mean angular acceleration is slightly smaller than the one obtained by the T scan due to a deterioration of the piezo inside the mount in-between the measurements.

and the newly obtained angular acceleration $\dot{\Omega}_M(T)$, allows the reconstruction of $\Omega_M(T)$ from the phases ϕ_{ij} . It should be noted here, that this additionally requires a good estimate of x_M and y_M , achievable by performing preceding calibration experiments using known mirror rotations or an additional imaging system. Here, we measure $x_M = 0.25$ m and $y_M = 1.5$ mm. Furthermore, we constrain the temporal change of the angular velocity, $\Omega_M = (\alpha(0) + \alpha(2T))/(2T)$ to be consistent with the angular acceleration, $\dot{\Omega}_M = (\alpha(0) - 2\alpha(T) + \alpha(2T))/T^2$, using the discrete samples of the mirror angle $\alpha(t)$ at times 0, T and $2T$. With this, we are able to reconstruct the shape of $\alpha(t)$ up to a constant offset. The resulting angular velocity and acceleration are depicted in Figure 3. We observe good agreement between the results obtained from fitting the interferometer phases and a direct measurement of the rotation, done by measuring the beams trajectory on a camera and calculating the relative angles to the original position of the beam. Only at larger interrogation times the angular velocity obtained from the atom interferometers is smaller than the direct measurement, potentially caused by the

diminishing contrast.

Differential measurement of angular acceleration - Here, we focus on a fixed interrogation time $T = 3.2$ ms (again including half of the beam splitter and mirror pulses) and scan the grid's y position by moving the mirror on a translation stage (see Figure 1) to obtain the average angular acceleration of the mirror's rotation. We rotate the mirror using the same piezo ramp as before, so we should obtain the same angular acceleration as previously for the specific T . This analysis is performed with a 2×3 BEC array, since the angular acceleration is acting column wise (eqn. 1) and perform two y scans with $(d_{x,1}, d_{y,1}) = (870, 390)$ μm and $(d_{x,2}, d_{y,2}) = (870, 580)$ μm . Shifting the stage in steps of $y_0 = 86.6$ μm results in a linear sweep of the phases, $\phi_{ij}(y_0) = 2k_{\text{eff}}T^2(y_{ij} - y_{M,0} + y_0)\dot{\Omega}_M(T) + \phi_{ij,0}(T)$ (see eq. (2)), where $y_{M,0}$ denotes the initial y distance between the BEC array's center and the mirror's center of rotation. The fringe scans $P_{ij}(y_0)$ are shown in Fig. 4. We overlap the signals of each column to showcase the column-wise agreement of the fringe scan's phase and frequency (different colors in 4), $P_{i,j}(y_0 + d_y) = P_{i,j+1}(y_0)$. The angular accelerations obtained from the fit are listed in Figure 4. The mismatch in frequency of the last column of the first measurement can be explained by clipping of the Bragg beam at the dichroic mirror splitting ODT and Bragg beam.

The angular acceleration measured here is smaller than the one obtained by scanning the pulse separation time (compare Fig. 3 b) and Fig. 4 (c), (d)). This offset can be attributed to an unintended change of the piezos position inside the mount between the measurements. We included the parametric plots of the data in the supplementary material.

Performance assessment - We assess the sensors uncertainties two-fold. On one hand, the uncertainty of linear acceleration measurements relies on the analysis of the individual sensitivities. On the other hand, gradiometry and gyroscopic measurements are based on differential signals between individual BECs, benefit from common-mode rejection, and thus involve only position-dependent noise sources.

Each individual BEC in the grid is sensitive to rotations and linear accelerations of the reference frame coinciding with the retroreflection mirror. The fundamental limit of the sensor's sensitivity to an acceleration a is given by $\delta a_{ij}^{\text{SN}} = \delta\phi_{ij}^{\text{SN}}/(2k_{\text{eff}}T^2)$ where $\delta\phi_{ij}^{\text{SN}} = 1/(C_{ij}\sqrt{N_{ij}})$ is the atomic shot noise limit. Here, C_{ij} denotes the contrast and N_{ij} the atom number of the (i, j) atom interferometer. With the experimental parameters given in Tab. I, we find $\delta a_{ij}^{\text{SN}} = 2.2 \times 10^{-5}$ m s^{-2} . Here, the sensor's linear acceleration signal is dominated by vibration noise, estimated to be of the order of 1×10^{-4} m s^{-2} .

In contrast, vibrational noise is suppressed in the differential measurement of linear acceleration gradients or

rotation rates. However, it requires the precise knowledge of the BECs' differential initial kinematics. Here, we correlate simultaneous phase measurements of multiple BECs at different positions to extract the acceleration gradient, rotation rates, and angular accelerations. This not only enables the simultaneous measurement of acceleration and rotation components, but allows the cancellation of common, i.e. position independent, noise sources. The shot noise limit for acceleration gradients γ is given by $\delta\gamma_{ij}^{\text{SN}} = \sqrt{\sum_{i,i+1}(\delta\phi_{ij})^2}/(2d_x k_{\text{eff}}T^2)$. Inserting the parameters in Tab. I, leads to a gradiometer sensitivity of $\delta\gamma_{ij}^{\text{SN}} = 7.2 \times 10^{-3}$ s^{-2} . To first order in T^2 , the angular velocity Ω and acceleration $\dot{\Omega}$ can be inferred by correlating phase measurements of BECs distributed along or transversely to the beam direction. The shot noise limits are $\delta\Omega_{ij}^{\text{SN}} = \sqrt{\sum_{i,i+1}(\delta\phi_{ij})^2}/(8d_x\Omega k_{\text{eff}}T^2)$ and $\delta\dot{\Omega}_{ij}^{\text{SN}} = \sqrt{\sum_{j,j+1}(\delta\phi_{ij})^2}/(2d_y k_{\text{eff}}T^2)$, respectively. Here, we find $\delta\Omega_{ij}^{\text{SN}} = 1.8 \times 10^{-3} \times \Omega$ and $\delta\dot{\Omega}_{ij}^{\text{SN}} = 1.8 \times 10^{-2}$ rad s^{-2} .

The overall sensitivity to inertial effects using the novel approach demonstrated here, is solely limited by technical constraints, such as vibration isolation levels, short baselines and the orientation control of the sensitive axis. Implementing further modifications to this setup, such as incorporating multiple loops or introducing an entirely different environmental context, would significantly enhance its sensitivity. The different sensitivity limits are estimated in Table I. Incorporating a relaunch mechanism and performing the interferometer over multiple loops would yield a reduction factor of the sensitivity limit of $1/\mathcal{N}_l$ with \mathcal{N}_l being the number of loops. Nevertheless, this would considerably diminish the contrast, thereby providing sensitivity gains anticipated to fall below the expected performance achievable in alternative environments. We further give estimations for the fundamental sensitivity limit of this sensor in different environments offering extended interrogation times, listed in Table I. Moving the apparatus into the Very Long Baseline Atom Interferometry (VLBAI) facility would give an estimated sensitivity gain of five orders of magnitude, showcasing the importance of the interrogation time. Further, advanced VLBAI or space-borne operation would yield even higher precision.

Conclusion and outlook - We have demonstrated the production of a 2D-BEC array of size up to 3×3 across 1.6 mm^2 utilising time-averaged optical potentials to realise an inertial measurement, measuring up to 3 quantities simultaneously. By correlating the phases of individual interferometers, we were able to measure the linear acceleration, angular velocity, and angular acceleration of the reference mirror. The linear acceleration caused by a slight tilt of the sensitive axis with respect to gravity was measured in a separate measurement. This ultimately facilitated the reproduction of the angular velocity, which had initially been too small to be visible in the row-wise differential phases. The

TABLE I. Shot noise limited sensitivity on linear accelerations (δa), acceleration gradients ($\delta\gamma$), angular velocities ($\delta\Omega$) and angular accelerations ($\delta\dot{\Omega}$) evaluated for different experimental configurations. We compare the approach presented here with optimized parameters offered by special facilities as the Very Long Baseline Atom Interferometer (VLBAI) [24], its advanced configuration (Adv. VLBAI), and typical parameters associated with a space-borne environment (Satellite) [29]. The uncertainty on $\delta\Omega$ is determined by the nominal angular velocity Ω , neglecting terms of the order $\mathcal{O}(\Omega\Omega T)$. Moreover, we assume a maximum separation of $(d_x, d_y) = (3, 1.2)$ mm for all platforms.

	2T [s]	N	C	δa [m s^{-2}]	$\delta\gamma$ [s^{-2}]	$\delta\Omega$	$\delta\dot{\Omega}$ [rad s^{-2}]
This publication	6×10^{-3}	10^4	0.8	2.2×10^{-5}	7.2×10^{-3}	$1.8 \times 10^{-3} \times \Omega$	1.8×10^{-2}
VLBAI	0.8	2×10^5	0.9	2.4×10^{-10}	8.0×10^{-8}	$2.0 \times 10^{-8} \times \Omega$	2.0×10^{-7}
Adv. VLBAI	2.8	1×10^6	1	4.0×10^{-12}	1.3×10^{-9}	$3.3 \times 10^{-10} \times \Omega$	3.3×10^{-9}
Satellite	9	10^5	1	3.8×10^{-13}	1.3×10^{-10}	$3.2 \times 10^{-11} \times \Omega$	3.2×10^{-10}

interrogation time in the present experiment is bounded to a few milliseconds because the BECs in use drop out of the horizontal atom optics light field, thus yielding a sensitivity limit of $\sim 10^{-4} \text{ m s}^{-2}$ for each interferometer in the array. We envision improved sensitivities using guided matter waves [5, 30]. Moreover, our method would greatly benefit from operation in long-baseline interferometers [23–25], where interrogation times on the order of seconds are accessible, thus enabling differential measurements of Earth’s rotation. It is worth pointing out that the continuous scalability of array spacings will enable detailed studies of systematic effects and scale factor calibrations. Finally, we anticipate exciting applications of our method for in-situ characterization of electromagnetic fields. Since each BEC effectively measures a local projection of the wave vector onto the gravitational acceleration, it becomes possible to systematically study wave front aberrations with high spatial resolution. Likewise, by observing Rabi oscillations and

step-wise translating the array, a full three-dimensional reconstruction of the light field may be realized.

Acknowledgements - This work is funded by the Federal Ministry of Education and Research (BMBF) through the funding program Photonics Research Germany under contract number 13N14875 and the Deutsche Forschungsgemeinschaft (DFG, German Research Foundation): Project-ID 274200144 - SFB 1227 DQ-mat (projects A05 and B07), Project-ID 434617780 - SFB 1464 TerraQ (project A02), and Germany’s Excellence Strategy - EXC-2123 QuantumFrontiers - Project-ID 390837967 and the German Space Agency at the German Aerospace Center (Deutsche Raumfahrtagentur im Deutschen Zentrum für Luft- und Raumfahrt, DLR) with funds provided by the German Federal Ministry of Economic Affairs and Climate Action due to an enactment of the German Bundestag under Grants No. 50WM2263A (CARIOQA-GE) and No. 50WM2253A (AI-Quadrat).

-
- [1] A. Peters, K. Y. Chung, and S. Chu, *Metrologia* **38**, 25 (2001).
- [2] J. M. McGuirk, G. T. Foster, J. B. Fixler, M. J. Snadden, and M. A. Kasevich, *Physical Review A* **65** (2002), 10.1103/physreva.65.033608, publisher: American Physical Society (APS).
- [3] G. Rosi, L. Cacciapuoti, F. Sorrentino, M. Menchetti, M. Prevedelli, and G. Tino, *Physical Review Letters* **114**, 013001 (2015), publisher: American Physical Society.
- [4] P. Asenbaum, C. Overstreet, T. Kovachy, D. Brown, J. Hogan, and M. Kasevich, *Phys. Rev. Lett.* **118**, 183602 (2017).
- [5] K. A. Krzyzanowska, J. Ferreras, C. Ryu, E. C. Samson, and M. G. Boshier, *Phys. Rev. A* **108**, 043305 (2023).
- [6] R. Gautier, M. Guessoum, L. A. Sidorenkov, Q. Bouton, A. Landragin, and R. Geiger, *Science Advances* **8**, eabn8009 (2022).
- [7] P. Berg, S. Abend, G. Tackmann, C. Schubert, E. Giese, W. P. Schleich, F. A. Narducci, W. Ertmer, and E. M. Rasel, *Phys. Rev. Lett.* **114**, 063002 (2015), publisher: American Physical Society.
- [8] J. K. Stockton, K. Takase, and M. A. Kasevich, *Physical Review Letters* **107**, 133001 (2011), publisher: American Physical Society.
- [9] B. Canuel, F. Leduc, D. Holleville, A. Gauguier, J. Fils, A. Viridis, A. Clairon, N. Dimarcq, C. J. Bordé, A. Landragin, and P. Bouyer, *Phys. Rev. Lett.* **97**, 010402 (2006), publisher: American Physical Society.
- [10] S. M. Dickerson, J. M. Hogan, A. Sugarbaker, D. M. S. Johnson, and M. A. Kasevich, *Physical Review Letters* **111** (2013), 10.1103/physrevlett.111.083001.
- [11] B. Barrett, P. Cheiney, B. Battelier, F. Napolitano, and P. Bouyer, *Phys. Rev. Lett.* **122**, 043604 (2019), publisher: American Physical Society.
- [12] M. Gersemann, M. Gebbe, S. Abend, C. Schubert, and E. M. Rasel, *The European Physical Journal D* **74**, 203 (2020).
- [13] Q. d’Armagnac de Castanet, C. D. Cognets, R. Arguel, S. Templier, V. Jarlaud, V. Ménéret, B. Desruelle, P. Bouyer, and B. Battelier, “Atom interferometry at arbitrary orientations and rotation rates,” (2024), arXiv:2402.18988 [physics.atom-ph].
- [14] S. Jose, P. Surendran, Y. Wang, I. Herrera, L. Krzemien, S. Whitlock, R. McLean, A. Sidorov, and P. Hannaford, *Physical Review A* **89** (2014), 10.1103/phys-

- reva.89.051602.
- [15] K. Gosar, V. P. Jevš enak, T. Mežnaršič, D. Babič, I. Poberaj, E. Zupanič, and P. Jeglič, *Physical Review A* **106** (2022), 10.1103/physreva.106.022604.
- [16] J. Nemirovsky, R. Weill, I. Meltzer, and Y. Sagi, “Atomic interferometer based on optical tweezers,” (2023), arXiv:2308.07768 [quant-ph].
- [17] R. Roy, A. Green, R. Bowler, and S. Gupta, *Phys. Rev. A* **93**, 043403 (2016).
- [18] G. Condon, M. Rabault, B. Barrett, L. Chichet, R. Arguel, H. Eneriz-Imaz, D. Naik, A. Bertoldi, B. Battelier, P. Bouyer, and A. Landragin, *Physical Review Letters* **123** (2019), 10.1103/physrevlett.123.240402.
- [19] A. Herbst, T. Estrampes, H. Albers, V. Vollenkemper, K. Stolzenberg, S. Bode, E. Charron, E. M. Rasel, N. Gaaloul, and D. Schlippert, *Phys. Rev. Res.* **6**, 013139 (2024).
- [20] H. Ahlers *et al.*, *Phys. Rev. Lett.* **116**, 173601 (2016).
- [21] A. Wanner, G. Bergmann, A. Bertolini, T. Fricke, H. Lück, C. M. Mow-Lowry, K. A. Strain, S. Gößler, and K. Danzmann, *Classical and Quantum Gravity* **29**, 245007 (2012), publisher: IOP Publishing.
- [22] N. Shettell and R. Dumke, “Emulating an Atomic Gyroscope with Multiple Accelerometers,” (2023), arXiv:2301.11155 [physics].
- [23] C. Overstreet, P. Asenbaum, J. Curti, M. Kim, and M. A. Kasevich, *Science* **375**, 226 (2022), publisher: American Association for the Advancement of Science.
- [24] D. Schlippert, C. Meiners, R. Rengelink, C. Schubert, D. Tell, É. Wodey, K. Zipfel, W. Ertmer, and E. Rasel, in *CPT and Lorentz Symmetry* (WORLD SCIENTIFIC, 2021).
- [25] L. Zhou, S.-T. Yan, Y.-H. Ji, C. He, J.-J. Jiang, Z. Hou, R.-D. Xu, Q. Wang, Z.-X. Li, D.-F. Gao, M. Liu, W.-T. Ni, J. Wang, and M.-S. Zhan, *Frontiers in Physics* **10** (2022).
- [26] H. Ahlers, L. Badurina, A. Bassi, B. Battelier, Q. Beaufiles, K. Bongs, P. Bouyer, C. Braxmaier, O. Buchmueller, M. Carlesso, E. Charron, M. L. Chiofalo, R. Corgier, S. Donadi, F. Droz, R. Ecoffet, J. Ellis, F. Estève, N. Gaaloul, D. Gerardi, E. Giese, J. Grosse, A. Hees, T. Hensel, W. Herr, P. Jetzer, G. Kleinsteiberg, C. Klempt, S. Lecomte, L. Lopes, S. Loriani, G. Métris, T. Martin, V. Martín, G. Müller, M. Nofrarias, F. P. D. Santos, E. M. Rasel, A. Robert, N. Saks, M. Salter, D. Schlippert, C. Schubert, T. Schuldt, C. F. Sopena, C. Struckmann, G. M. Tino, T. Valenzuela, W. von Klitzing, L. Wörner, P. Wolf, N. Yu, and M. Zelan, “STE-QUEST: Space Time Explorer and QUantum Equivalence principle Space Test,” (2022), arXiv:2211.15412 [gr-qc, physics:hep-ex, physics:hep-ph, physics:physics, physics:quant-ph].
- [27] Q. Beaufiles, J. Lefebvre, J. G. Baptista, R. Piccon, V. Cambier, L. A. Sidorenkov, C. Fallet, T. Lévêque, S. Merlet, and F. Pereira Dos Santos, *npj Microgravity* **9**, 53 (2023).
- [28] R. Li *et al.*, (In preparation).
- [29] C. Struckmann, R. Corgier, S. Loriani, G. Kleinsteiberg, N. Gox, E. Giese, G. Métris, N. Gaaloul, and P. Wolf, *Phys. Rev. D* **109**, 064010 (2024).
- [30] G. McDonald, C. Kuhn, S. Bennetts, J. Debs, K. Hardman, J. Close, and N. Robins, *Eur. Phys. Lett.* **105**, 63001 (2014).
- [31] M. Kasevich and S. Chu, *Phys. Rev. Lett.* **67**, 181 (1991).
- [32] E. Torrontegui, S. Ibáñez, X. Chen, A. Ruschhaupt, D. Guéry-Odelin, and J. G. Muga, *Phys. Rev. A* **83**, 013415 (2011).
- [33] H.-R. Noh, S. E. Park, L. Z. Li, J.-D. Park, and C.-H. Cho, *Opt. Express* **19**, 23444 (2011).
- [34] R. H. Parker, C. Yu, B. Estey, W. Zhong, E. Huang, and H. Müller, *Phys. Rev. A* **94**, 053618 (2016).

I. SUPPLEMENTAL MATERIAL

Setup ODT - Key feature of the experimental setup is the optical dipole trap (ODT) setup. The BEC array is created in a sectional plane of both ODT beams in x/y-direction (see Fig. 1). The beam is collimated and split into two beam paths (BP1/2) 1. The two beams differ in power and beam waist in the center of the experimental chamber - BP1 has a power of 3.5 W and a beam waist of 22 μm . BP2 has 30 W of power and a beam waist of 80 μm

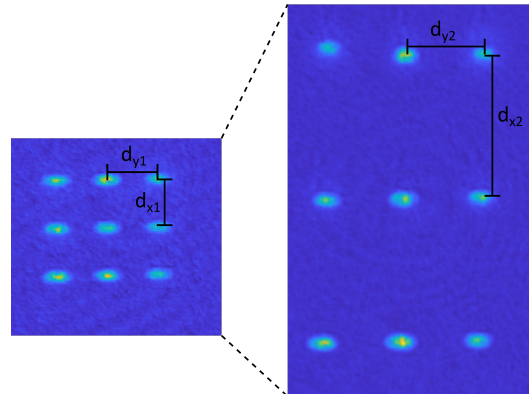


FIG. S1. **Absorption images prior to and after the transport ramp.** The distances $d_{x1/y1}$ are increased to $d_{x2/y2}$ after applying the sigmoidal frequency ramps shown in I.

in x-direction. One 2D-acousto optical deflector (AOD) (DTSXY-400) per beam path enables control of the position, amplitude and number of modes in the crossed ODT. The AODs are fed signals generated by a software defined radio (SDR) in the horizontal directions. The software to drive the SDR is custom made and tailored to the experiment. By applying simultaneously multiple frequency ramps to the AODs distinct harmonic wells in the form of a 2D-array can be created.

Hybrid trap & Optical evaporation - Starting point of the production of the 2D-BEC array is a precooled ensemble of $\sim 1 \times 10^9$ ^{87}Rb atoms with a temperature of 560 μK in a magnetic trap. Using a microwave (MW) knife [S31] the atoms are evaporatively cooled and after 1.05 s of evaporation a temperature of 150 μK is reached. At this point the ODT is switched on with maximum power. After another 800 ms the magnetic field gradient is decreased to 78 G cm^{-1} and further MW knife evaporation yields an ensemble consisting of $1 - 1.5 \times 10^8$ atoms at a temperature of 50 μK . The atoms transferred into the crossed ODT are now cooled to BEC by optical evaporation. This is done by using three modes in each of the two beam paths. They have a spatial position of -97, 48.5, 194 μm in y and -511.2, -319.5, -127.8 μm in x towards the camera taking absorption images in z-direction, coaligned with gravity. After 2.55 s of all optical evaporation the cooling sequence is completed with temperatures of the samples ranging from 6 - 9 nK. Pow-

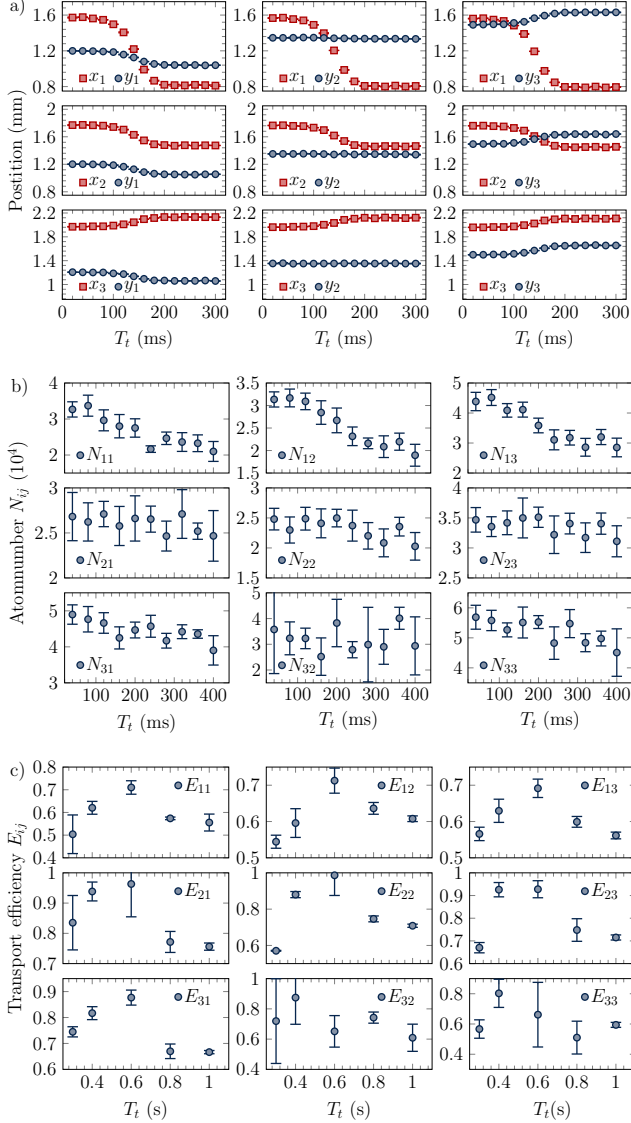


FIG. S2. **Characterisation of a transport ramp for the 3×3 -array.** **a)** Trajectories for the 9 BECs moving in x/y -direction (red/blue). The resulting grid has a spacing of $d_{x/y} = 600/300 \mu\text{m}$. **b)** Atom numbers in the BECs for a 400 ms transport ramp. **c)** Efficiencies of the transport, meaning the atom number at the start of the ramp divided by the atom number at the end of the transport ramp.

ers in the ODT beams were exponentially ramped down to 85 mW (BP1) and 437 mW (BP2). The atom number in the resulting 3×3 2D-BEC array is 3.5×10^5 . The BEC grid has spatial separation of $d_{x/y} = 191 / 48.5 \mu\text{m}$ in the x / y - plane.

State preparation & Optical transport - For state preparing the ensembles in the $|F = 1, m_F = 0\rangle$ a sequence of Rabi- π pulses of the MW is used. Active magnetic field stabilisation in z -direction compensates for

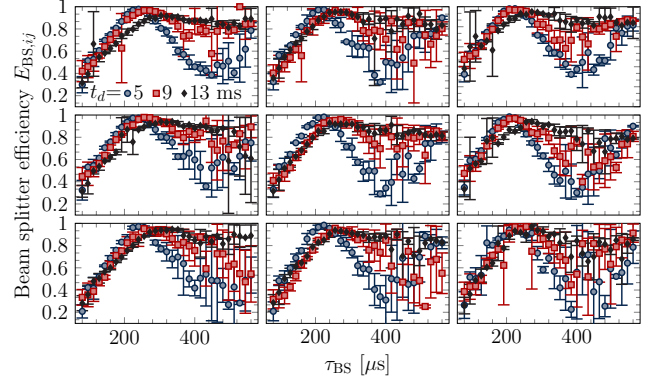


FIG. S3. **Rabi oscillations of the double Bragg diffraction.** The oscillations were measured by scanning the pulse duration τ_{BS} for different pre ToFs t_d . Since the atoms fall through the Bragg beam with a diameter of 6.5 mm the oscillation retards and the efficiency drops as t_d increases. The array had dimensions of $d_{x/y} = 660/290 \mu\text{m}$.

earth's magnetic field and lifts degeneracy of the hyperfine levels with $B_z = 3.69$ G. The state preparation has an efficiency of > 0.95 and remaining atoms in the magnetic sensitive states are removed by pulsing on the magnetic field for one second. For transporting the ensembles sigmoidal frequency ramps are applied to the AODs [S32], effectively stretching the array. The final positions of the BECs is set to $-242.5, 48.5, 339.5 \mu\text{m}$ in y - and $-660.3, -21.3, -617.7 \mu\text{m}$ in x -direction. In Fig. I a) the trajectories of the BECs in the x/y -direction are displayed. The resulting 3×3 -grid has a spacing of $d_{x/y} = 600/300 \mu\text{m}$. In Fig. I b) the atom number of each BEC is shown for a transportation time of 400 ms is shown. The efficiencies E_{ij} of the transport ramps range from .6 to .95 depending on the transported distance (Fig. I c)). For transportation ramps with transport time $T_t > 600$ ms lifetime losses dominate. We observe differing trapping frequencies which can be explained by different amplitudes of the RF-signal fed to the AOD and a tilt in the sectional plane of the two laser beams. The trap frequency measurement yields following values for the trap frequencies in $x / y / z$ [Hz]: 93.7, 100.1, 104.4, 115.1, 122.5, 126.8, 128.9, 136.9, 139.6 / 17.6, 24.8, 28.6, 24.7, 28.6, 30.3, 23.3, 28.6, 30.5 / 176.9, 170.4, 176.2, 149.0, 157.9, 165.3, 138.5, ?, ? for the BECs 1 – 9. For the measurement of the trap frequency in z -direction fluorescence detection was used such that not all nine ensembles were sufficiently resolved. This is why ensemble (3,2) and (3,3) are missing. The now well separated BEC grid can be used for atom interferometry. **Interferometry setup** - The light pulses to drive the $\pi/2$ - and π -pulses of the interferometer are double-Bragg diffraction pulses [ref]. We use a frequency doubled Lumibird Keopsys CEFL-KILO MOPA (BL) with output power of 200 mW for interferometry and for referencing the other two cooling lasers that are used for the cool-

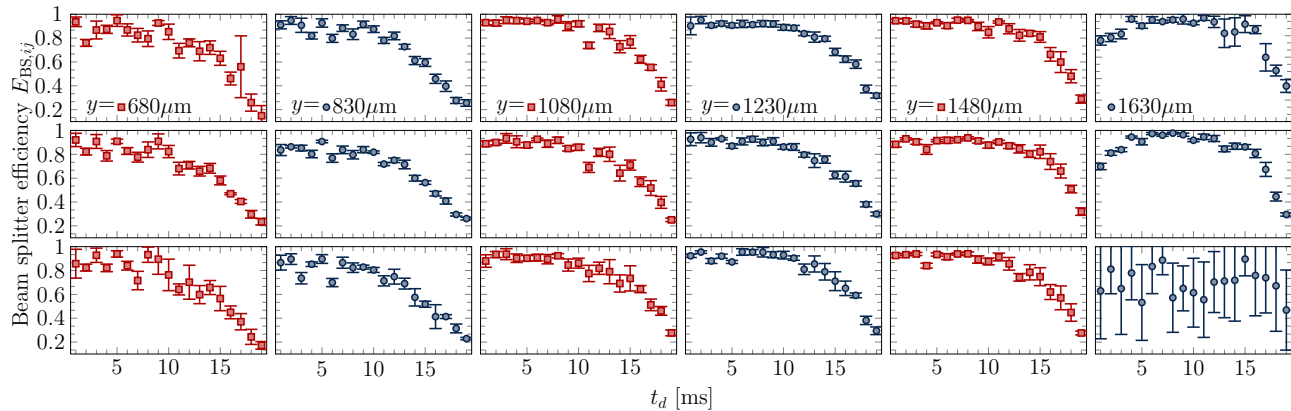


FIG. S4. **Pulse efficiency for different y-positions.** By shifting the array by $150\mu\text{m}$ and scanning the pre ToF t_d the splitting efficiency was mapped transversal to the Bragg-beam. The efficiency drops from right to left, meaning that the array was shifted to the left regarding the Bragg-beams center.

ing steps prior to the ODT. It is locked to the ^{85}Rb cooling transition via modulation transfer spectroscopy [S33]. A total of 120 mW is fed into the system and first split at a polarisation beam splitter (PBS). Both beams are thereafter diffracted with two AOMs driven at 200 and 200.015 MHz and the first orders are recombined at a second PBS to overlap them and ensure orthogonal polarisations. Before feeding them into a fiber leading to the experiment, they are fed through another AOM for switching. The RF-signal fed into this AOM has a gaussian amplitude, for optimal efficiencies of the Bragg-pulses [S34]. A total of 12 mW in both beams is transferred to the experimental chamber. The beam is collimated to 6.5 mm beam diameter and coaligned with BP1 of the ODT. After passing through the chamber a dichroic mirror is used to separate ODT and Bragg beam. The Bragg beam is passing a $\lambda/4$ -plate and is retro reflected at a mirror, rotating the polarity of both back reflected beam components by $\pi/2$. This enables Double-Bragg driven atom interferometry with momentum transfer $\pm 2\hbar k_{\text{eff}}$. The beam splitter/mirror pulse has an efficiency of .95/.80 (see Fig. I depicting Rabi-oscillations of the beam splitter). The retro reflection mirror is glued to a 3D-printed mount housing a Thorlabs APF503 piezo (red box in Fig. 1). By applying suitable voltage ramps during the interferometry sequence, the mirror can be tilted in x-direction resulting in an effective rotation of the mirror around the z-axis. The mirror is moreover tilted in z-Axis by an angle $\beta < 3^\circ$ to induce accelerations $a_x = g \times \sin \beta$, with the gravitational acceleration g . The interferometry pulses are applied after

transport and another 1 s of wait time, to calm down any excitations induced by the transport. The ODT beams are switched off and the atoms are free falling in z-direction. After a pre time of flight (ToF) t_d we apply the first interferometry pulse, starting the interferometer sequence.

Bragg Diffraction - Since the laser light used for the Bragg-transitions is a gaussian profile with a diameter of 6 mm, collimated with a telescope before passing the experimental chamber, the intensity of the gaussian profile can be sampled with the 2D-array. This is due to the Rabi-frequency being proportional to $\sqrt{I_1 I_2}$ of the two components of the light field [ref]. For characterising the beam splitter, two measurements were made: In the first (see fig. I) the pulse duration τ_{BS} was scanned for different pre ToF times $t_d = 5, 9, 13$ ms, resulting in a retardation and lower amplitude of the Rabi-frequency for longer t_d s. The second measurement was taken for optimal pulse duration τ_{BS} , but the pre ToF t_d was scanned. The 2D-array was shifted for the second run of the experiment by $150\mu\text{m}$ in y-direction indicated by the two colors blue/red in fig. I. A rise of efficiency from small to big y-values indicates that the Bragg-beam's center is located at the rightmost column of the measurement or even further to the right. However, the Bragg-beam could not be moved further to the left, due to clipping at the 1'-dichroic mirror separating Bragg- and dipole trap beam. **Differential measurement of angular acceleration** - Another way to plot the data in Fig. 4 is to plot it parametrically. The thereby created ellipses are visible in Fig. I and correspond to the phase shifts of the sinusoidal signals depicted in 4.

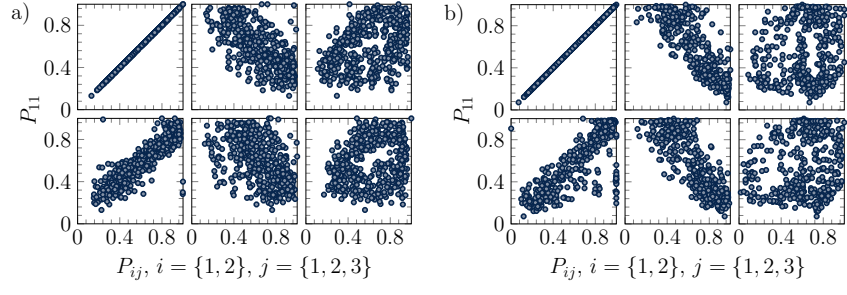


FIG. S5. **Parametric plots of the differential measurement of angular acceleration a/b)** Parametric plots of the data shown in 4 a)/b).